Particle Segregation in Falling Polydisperse Suspension Droplets

Melissa Faletra and Jeffrey S. Marshall
School of Engineering, The University of Vermont, Burlington, Vermont, U.S.A.

and

Mengmeng Yang and Shuiqing Li
Key Laboratory for Thermal Science and Power Engineering of Ministry of Education
Department of Thermal Engineering, Tsinghua University, Beijing, China

Corresponding Author: Jeffrey S. Marshall, School of Engineering, The University of Vermont, Burlington, VT 05405, U.S.A.
PHONE: 1 (802) 656-3826, EMAIL: jmarsha1@uvm.edu.

Keywords: Particle cloud; particle flows; Oseenlet flows

Abstract

The problem of a suspension droplet falling under gravity was examined for polydisperse droplets composed of a mixture of particles with different densities and sizes. The study was conducted using both simulations based on oseenlet particle interactions and laboratory experiments. It was observed that the hydrodynamic interactions of the particles within the suspension droplet allow a polydisperse collection of particles to fall as a coherent droplet, even for cases where the difference in particle terminal velocity would cause them to quickly separate from each other in the absence of hydrodynamic interactions. However, a gradual segregation phenomenon is observed in which lighter/smaller particles (with lower terminal velocity) preferentially leave the suspension droplet by entering into the droplet tail, whereas heavier/larger particles (with higher terminal velocity) remain for longer periods of time within the droplet. When computations and experiments are performed for bidisperse mixtures, with two particle densities or two particle sizes, a point is eventually reached where all of the lighter/smaller particles are ejected into the droplet tail and the droplet continues to fall with only the heavier/larger particles.

1. Introduction

A *suspension droplet* is a cluster of particles held in suspension in a surrounding fluid. If the particle density is different from that of the surrounding fluid, the suspension droplet either falls or rises (for heavier or lighter particles, respectively) in the presence of a gravitational field. This problem has generated significant interest in the fluid mechanics community in part because it is an apparently simple problem that leads to highly complex and interesting dynamics and in part because at sufficiently high particle concentrations, it is a flow field that is dominated by the hydrodynamic interaction between the particles. The problem is relevant to a number of geophysical and environmental applications in which clusters of heavy particles generate turbulence as they sink in a lighter fluid. For instance, in direct numerical simulations of homogeneous turbulence of a particulate fluid under gravity, Elgobashi and Truesdell (1993) found that turbulence generation by falling groups of particles was a primary source of turbulence generation. Similar physics occurs for buoyant plumes of particles that are lighter than the surrounding fluid (Hurley and Physick, 1993). Suspension droplet dynamics is also relevant to applications involving smoke inhalation in the human lung. A number of investigators have observed that in cases with high particle concentrations, the penetration of particles into the lung in inhaled cigarette smoke is significantly greater than predicted based on single-particle settling velocities (Martonen, 1992; Phalen et al., 1994; Robinson and Yu, 2001). One explanation that has been proposed for this difference is that smoke particles move through the upper airway region in the form of a suspension cloud, where the hydrodynamic interaction of particles within this cloud allows the particles to travel more rapidly relative to the surrounding fluid than would be

the case for isolated particles. The ability to accurately model the degree of penetration of particles into the lung is very important in understanding the health effects of inhaling cigarette smoke, as well as related problems of inhalable drug dispersal and silicon dust inhalation in construction and mining operations.

The dynamics of a small number of settling particles falling under gravity has been examined in a number of studies (Bretherton, 1964; Jataweera et al., 1964; Hocking, 1964; Vasseur and Cox, 1977; Ekiel-Jeżewska and Felderhof, 2005, 2006a), which have lead to identification of different stable and unstable particle configurations. As the number of particles increases, dynamical systems approaches become increasingly difficult and the problem must instead be approached as one of suspension dynamics, although computational approaches continue to solve for the system at the individual particle level. The droplet dynamics is typically characterized by two different Reynolds numbers, called the droplet Reynolds number $\mathrm{Re}_d = 2r_d U_{d,HR}/\nu$ (also sometimes called the cloud Reynolds number) and the particle Reynolds number $\mathrm{Re}_p = 2r_p U/\nu$. Here, r_p and r_d are the particle and droplet radii, respectively, ν is the fluid kinematic viscosity, $U_{d,HR}$ is a theoretical estimate of the droplet settling velocity based on the initial number of particles in the droplet, and U is the settling velocity of an isolated particle in an otherwise stagnant fluid.

The settling of an initially spherical particle suspension droplet under gravity was examined by Nitsche and Batchelor (1997) low Reynolds-number clouds using both experiments and numerical simulations. The numerical simulations were performed by representing each particle by the sum of a stokeslet and a doublet that induce a velocity field on all other particles. This computational approach requires that both the droplet and

the particle Reynolds numbers are small compared to unity. Nitsche and Batchelor observed that the suspension droplet settles significantly more rapidly than would be predicted for a cloud of non-interacting particles due to the fluid motion induced by the particle settling. They also showed that a reasonable approximation for the suspension droplet settling velocity can be obtained from the Hadamard-Rybczyński (HR) solution for a spherical droplet of an immiscible fluid immersed in another fluid at low Reynolds number (see also Ekiel-Jeżewska et al., 2006b).

As the suspension droplet falls downward, a series of transitions in the flow pattern takes place (Adachi et al., 1978; Noh and Fernando, 1993). As originally described by Adachi et al (1978), the particle cloud in certain cases adopts a toroidal shape which breaks up into some number of offspring droplets, where the offspring droplets then repeat this process. The evolution of a suspension droplet into a toroidal shape is analogous to a similar process that occurs for a droplet of a heavy liquid immersed in a lighter liquid (Kojima et al., 1984). These transitions were examined in detail both experimentally and using stokeslet-based simulations by Machu et al. (2001) and Metzger et al. (2007) for low Reynolds number droplets with spherical particles and by Park et al. (2010) for suspensions formed of fibers.

Subramanian and Koch (2008) examine different regimes of suspension droplet dynamics based on the particle Reynolds number the particle concentration, and the droplet size. They argue that for cases where the particle Reynolds number and the particle concentration are small, but the droplet Reynolds number is not small, a more accurate computational approach is obtained by replacing the stokeslet and the potential doublet in the simulation approach of Nitsche and Batchelor with the steady Oseen

solution for flow past a sphere. This oseenlet-based approach was used by Pignatel et al. (2011), along with experiments, to explore suspension droplet dynamics at finite droplet Reynolds numbers. Other computational methods have also been used to examine suspension droplet flows. For instance, Bosse et al (2005) approximated the fluid-particle interaction force as a distributed body force on a grid, from which they solved for the induced flow field using a pseudo-spectral technique. Chen and Marshall (1999) employed a vorticity-based method in which the curl of the fluid-particle interaction force acts as a source term in the vorticity transport equation. The solution was obtained (in two dimensions) using a Lagrangian approach that employed a combination of vortex blobs and point particles. A related vorticity-based method was employed in three dimensions by Walter and Koumoutsakos (2001), in which a vortex-in-cell method was used to compute the velocity field.

All of the papers described above consider suspensions formed of monodisperse particles, with uniform particle diameter, density, etc. In a polydisperse mixture, with variation in particle properties differ, the sedimentation process will generally lead to particle segregation due to differences in particle settling velocity. Consequently, the particles within a settling polydisperse suspension droplet would rapidly segregate in the absence hydrodynamic interaction between the particles. In the presence of hydrodynamic interaction, the recirculating flow field within the suspension droplet acts to inhibit particle segregation, provided that the heterogeneities between the particles are sufficiently small and the particle concentration sufficiently high. Similar inhibition of particle segregation in a mixture due to particle hydrodynamic interaction was noted by Roeder et al. (1995) in a centrifugal flow field.

The current paper uses a combination of oseenlet-based simulations and laboratory experiments to examine the dynamics of falling polydisperse suspension droplets. The simulations and experiments are both subject to a number of limitations, and as a consequence cover somewhat different regimes of suspension droplet motion. Specifically, the oseenlet-based computation method (like the stokeslet-based method used for vanishing Re_d) is valid only for small particle concentrations and small particle Reynolds numbers Re_p. In the experiments, we seek to initialize the flow field as a sphere of well-mixed polydisperse particles in a stationary liquid bath. A cluster of particles placed at the top of the liquid bath is observed to form a structure that reasonably resembles this idealization at sufficiently low droplet Reynolds numbers and high particle concentrations; however, at low particle concentrations, we have experienced difficulty in obtaining a well-mixed spherical structure at the onset of the experiments. These limitations force the simulations to focus on low concentration clusters and the experiments to focus on high concentration clusters, although both approaches have values of the droplet Reynolds number near unity and both are conducted at small particle Reynolds numbers. It is of interest that despite the differences in particle concentration, both experiments and computations exhibit a similar mechanism leading to particle segregation from the suspension droplet.

The computational method used in the paper is described in Section 2a, followed by a summary of computational results for monodisperse and polydisperse mixtures. We have examined a wide assortment of polydisperse mixtures, including bidisperse mixtures with two different particle densities, bidisperse mixtures with two different particle sizes, and polydisperse mixtures with a distribution of particle size and density. The mechanics

in all cases examined are similar, depending only on differences in the particle terminal velocity. For brevity, Section 2 focuses on bidisperse mixtures with two different particle densities. An experimental investigation is presented in Section 3 for settling of suspension clouds with bidisperse particle mixtures with particles of different sizes and densities. Conclusions are presented in Section 4.

2. Computational Method and Results

2.1. Oseenlet Simulation Method for Particle Hydrodynamic Interaction

Computation of the particle interactions using stokeslets requires that both the particle Reynolds number Re_p and the cloud Reynolds number Re_d be small compared to unity. The latter restriction arises from the fact that the Stokes equation is only valid within distances from the particle centroid that are small compared to the inertial screening length $\ell = r_p / \mathrm{Re}_p$. A uniformly valid solution for the flow around a particle with low particle Reynolds number is given by the Oseen solution (Proudman and Pearson, 1957), from which the flow field generated by a spherical particle with radius r_p translating with a velocity $U_S \mathbf{e}_x$ relative to the surrounding fluid at low particle Reynolds number can be written in a local spherical coordinate system, with the polar axis ($\theta = 0$) coincident with the direction of particle motion, as

$$u_r = \frac{U_S r_p^2}{r^2}\left\{-\frac{r_p}{2r}\cos\theta - \frac{3(1-\cos\theta)r}{4r_p}\exp\left[-\frac{\mathrm{Re}_S\, r(1+\cos\theta)}{2r_p}\right] + \frac{3}{2\,\mathrm{Re}_p}\left(1-\exp\left[-\frac{\mathrm{Re}_S\, r(1+\cos\theta)}{2r_p}\right]\right)\right\}$$

$$u_\theta = -\frac{U_S r_p}{r}\sin\theta\left(\frac{r_p^2}{4r^2}+\frac{3}{4}\exp\left[-\frac{\mathrm{Re}_S\, r(1+\cos\theta)}{2r_p}\right]\right). \qquad (1)$$

In this equation, $\mathrm{Re}_S = 2r_p U_S/\nu$ is the instantaneous particle Reynolds number based on the particle slip velocity $U_S \equiv |\mathbf{v}-\mathbf{u}|$, where **v** is the particle velocity and **u** is the fluid velocity at the particle centroid (evaluated as if the particle were not present). This solution approaches the Stokes solution for flow past a sphere within a region $r << \ell$ near to the particle, but at large distances $r >> \ell$ the velocity field approaches that of a potential point source, with decay rate of $O(1/r^2)$. The fluid emitted from this source is recovered in a back-flow region located within a thin wake near $\theta = \pi$, within which the velocity magnitude decays as $O(1/r)$.

The fluid velocity $\mathbf{u}_i$ at the centroid of particle *i*, where *i* = 1,...,*N*, is obtained at each time step by solution of a matrix equation of the form

$$\mathbf{u}_i = \sum_{j\neq i} \mathbf{W}(\mathbf{x}_i,\mathbf{x}_j)(\mathbf{v}_j - \mathbf{u}_j). \qquad (2)$$

The matrix **W** is obtained using (1) after rotating the local spherical coordinate system into a global coordinate frame. Since the particle Stokes number is vey small in the current simulations, we adopt the same assumption used by numerous previous investigators (Nitsche & Batchelor, 1997; Subramanian & Koch, 2008; Pignatel et al., 2011) that the particle inertia is negligible, so that the fluid slip velocity U_S is set equal

to the particle terminal velocity U in an otherwise stationary fluid (and Re_S and Re_p become identical).

The governing equations for the suspension droplet motion can be non-dimensionalized by selecting the characteristic fluid length and velocity scales as the initial droplet diameter L and the terminal settling speed U of an isolated particle of nominal size and density, where the latter is given by

$$U = \frac{d^2 g_R}{18\nu\chi}, \tag{3}$$

and $g_R = (1-\chi)g$ is the reduced gravitational acceleration and $\chi = \rho_f / \rho_p$ is the density ratio. For computations with variable size and density particles, it is convenient to define a nominal particle density $\overline{\rho}_p$ and diameter $\overline{d}$ by

$$\overline{\rho}_p = \frac{1}{N}\sum_{n=1}^{N} \rho_n \ , \qquad \overline{d} = \left(\frac{1}{N}\sum_{n=1}^{N} d_n^2 \right)^{1/2}, \tag{4}$$

where N is the total number of particles. The nominal particle diameter is specified by averaging the square of the diameter to ensure that the average terminal velocity (for an isolated particle) will be equal to that for particles whose diameter are equal to the nominal value $\overline{d}$. For a mixture, the density ratio $\chi = \rho_f / \overline{\rho}_p$ is based on the nominal particle density. The Froude number $\mathrm{Fr} = U / \sqrt{g_R L}$ and the Stokes number

$\mathrm{St} = \overline{\rho}_p \overline{d}^2 U / 18\mu L$ for this flow can be expressed in terms of the particle Reynolds number as

$$\mathrm{St} = \mathrm{Fr}^2 = \frac{\mathrm{Re}_p}{18\chi}(\overline{d}/L). \tag{5}$$

The results plotted in the paper are in terms of dimensionless variables in which all length scales are nondimensionalized by the droplet diameter L, all velocity scales are nondimensionalized by particle terminal velocity U (computed using (3) with the nominal particle diameter and density), and all time scales are nondimensionalized using L/U. Dimensionless variables are denoted by an asterisk.

2.2. Suspension Droplets with Monodisperse Particles

For monodisperse particles, the independent dimensionless parameters of the flow include droplet Reynolds number Re_d, dimensionless particle diameter $\varepsilon \equiv \overline{d}/L$, density ratio $\chi = \rho_f / \rho_p$, and the initial number of particles N_0 contained within the droplet. Several previous studies of monodisperse suspension droplets have been reported which detail how the droplet fall velocity and shape change with variation of these parameters (Nitsche & Batchelor, 1997; Metzger et al., 2007; Subramanian & Koch, 2008; Pignatel et al., 2011). An important characteristic noted in this literature is the tendency of the falling suspension droplet to develop a tail formed of particles that leak away from the droplet near the droplet rear.

Results are reported in the current section for a case with $\mathrm{Re}_d = 1.4$, $\bar{d}/L = 0.04$, $\chi = 1/3$, and $N_0 = 300$, which serves as a baseline for the polydisperse droplet simulations. The initial particle concentration is given by $\phi_0 = N_0(\bar{d}/L)^3 \cong 0.019$ and the particle Reynolds number is $\mathrm{Re}_p = 0.004$, so the conditions required for use of the oseenlet simulation approach are well satisfied. A time series showing formation of the droplet tail for this baseline case is given in figure 1. The suspension droplet initially has the form of a sphere, but a tail of trailing particles shed from the rear of the droplet gradually develops. The tail grows progressively longer with time since the particles within the tail fall at nearly the terminal velocity for an isolated particle, whereas the particles within the droplet fall at a much faster speed due to the hydrodynamic interaction between the particles. The droplet shape becomes deformed in time, with a slight flattening of the ball-like shape in the vertical direction. The fluid velocity field in a frame traveling with the droplet is similar to that shown by Pignatel et al. (2011). The flow surrounding the droplet has a toroidal structure qualitatively similar to a Hill's spherical vortex, with stagnation points at the front and back.

The dimensionless fall velocity of the particles within the droplet, U_d^*, and the current number of particles in the droplet, $N(t)$, are plotted in figure 2 as functions of dimensionless time. In order to allow some deformation of the suspension droplet, we use an effective droplet diameter equal to 1.25 to determine which particles are in the droplet, which is 25% larger than the nominal droplet diameter. All particles are observed to fall within the droplet for a short time at the beginning of the computation (approximately $t^* < 0.5$), following which formation of the droplet tail leads to a gradual decrease in

number of particles within the droplet. The fall velocity reaches a maximum value at about $t^* = 0.5$, which is also the time at which the particle tail starts to form. The peak magnitude of the fall velocity is substantially greater than unity, indicating that the suspension droplet falls much faster than an isolated particle. The droplet fall velocity decreases for dimensionless times t^* greater than 0.5 as the particles gradually move from the droplet into the tail and the tail grows progressively longer.

A simple theoretical expression for droplet fall velocity is obtained by treating the particle suspension as a droplet of another (immiscible) fluid with effective density ρ_d and viscosity μ_d. The solution for drag on a fluid droplet suspended in an immiscible liquid was given independently by Hadamard (1911) and Rybczynski (1911) as

$$U_{d,HR} = \frac{(\rho_d - \rho_f) g L^2}{12 \mu_f} \left(\frac{\mu_f + \mu_d}{\mu_f + \frac{3}{2}\mu_d} \right). \tag{6}$$

The density difference in (6) can be written in terms of the particle volume concentration $\phi = N\varepsilon^3$ within the droplet as $\rho_d - \rho_f = \phi(\rho_p - \rho_f)$. The effective viscosity is given for small concentrations by the Einstein expression

$$\mu_d = \mu_f (1 + \tfrac{5}{2}\phi). \tag{7}$$

Linearizing (6) for small concentration values and dividing by the isolated particle fall velocity U yields

$$U^*_{d,HR} \equiv \frac{U_{d,HR}}{U} = \frac{6}{5} N\varepsilon \,, \tag{8}$$

where N is the number of particles in the droplet. A plot of the ratio $U^*_d(t)/[\frac{6}{5}N(t)\varepsilon]$ of the computed and theoretical droplet fall velocity as a function of time is given in figure 2c. The computed value of this ratio is initially close to unity, and then it decreases gradually in time to about 0.9. The oscillations in value of this ratio observed in the figure are a consequence of shape oscillations of the suspension droplet. The computed velocity value shown in figure 2 is close to that obtained both experimentally and computationally by Pignatel et al. (2011).

Two measures of the length of the particle tail are shown in figure 3 – the root-mean-square position y^*_{rms} of the particles in the y-direction and the ratio $(y^*_{\max} - y^*_{\min})/4$. For particles that are uniformly distributed between $y^*_{\max}$ and $y^*_{\min}$, these two measures would be equal, so the difference between these measures provides an indication of the skewness of the particle distribution. The value of y^*_{rms} remains close to the value for a uniform sphere for $t^* < 1$, after which the growth of the droplet tail causes y^*_{rms} to increase nearly linearly with time. The value of $(y^*_{\max} - y^*_{\min})/4$ is larger than the corresponding value of y^*_{rms}, as presence of the droplet implies a large number of particles with values of y^* near $y^*_{\min}$. Over time, the two measures approach each other as an increasing number of the particles are drawn out into the tail region.

2.3. Suspension Droplets with Polydisperse Particles

Computations for a wide range of polydisperse suspension droplets have been conducted, including a series of cases with particles of two different sizes, a series with particles with two different densities, and many flows with a distribution of both particle size and density. All of the cases examined exhibited the same essential physics, which seems to depend on the difference in value of particle terminal velocity rather than which specific property is varied. For the sake of brevity, the current section presents polydisperse suspension droplet results for a representative series of cases where half the particles have one density value and the other half have a different density value. The particle polydispersity can be characterized by a dimensionless parameter $\beta \equiv \left|\rho_{p2} - \rho_{p1}\right| / 2\overline{\rho}_p$. A full report of the different computational cases examined is given in the thesis by Faletra (2014).

We begin by examining the effect of droplet concentration on the segregation phenomenon by simulating droplet settling for cases in which the initial number of particles N_0 varies between 50 and 1000, where all other parameters are held constant at $\beta = 0.5$, $\overline{d} / L = 0.04$, $\chi = 1/3$, $\mathrm{Re}_d = 1.4$, and $\mathrm{Re}_p = 0.004$. A typical case in which particle hydrodynamic interaction has a strong effect on inhibiting particle segregation is that of $N_0 = 300$. The early evolution of the droplet in this case is shown in a time series in figure 4. Similar to the simulations for monodisperse particles, the suspension droplet falls with nearly a spherical shape with a tail of trailing particles shed from the rear of the droplet. As time passes, the tail grows progressively longer because the particles in the tail fall at approximately the terminal velocity of an isolated particle, whereas the particles in the droplet fall much faster due to the hydrodynamic interaction between the particles in the droplet. Due to the strong particle hydrodynamic interactions, some of the

light particles are able to remain inside the suspension droplet for a long period of time. At the same time, it is clear that the lighter particles have a much higher probability of passing into the drolet tail than do the heavier particles, particularly near the start of the computation. The heavier particles do eventually start to enter into the tail, but at a lower rate than the lighter particles. At long time, a point is reached where all of the light particles are removed from the droplet and form a very long tail, after which the rate at which particles enter into the tail decreases significantly.

For small numbers of particles (e.g., $N_0 = 50$ or 100), the weak hydrodynamic interaction between the particles is insufficient to significantly slow down the separation of light and heavy particles that occurs due to the difference in terminal velocity. The particles of the two densities separate as two dispersed clouds before the suspension droplet has fallen more then a few droplet diameters. A comparison of cases with different initial concentration values is given in figure 5, in which the percentage of initial particles that remain in the droplet is plotted as a function of time for cases with $N_0 = 50$, 100, 300, and 1000. These percentages are shown separately for the light particles and the heavy particles. The results for cases with $N_0 = 50$ and 100 are almost the same, and both are typical of cases in which the amount of hydrodynamic interaction is too small to significantly inhibit particle segregation. Increase in value of N_0 above 100 results in delay of the separation of light particles from the droplet and increase in the rate of separation of heavy particles from the droplet. The delay in separation of light particles is due to the strong recirculating flow surrounding the droplet, which acts to suspend particles with different terminal velocities. The increase in rate of transport of the heavier particles into the tail for large values of N_0 is opposite to the trends observed

for leakage rate in monodisperse suspension droplets, for which the leakage rate decreases with increase in N_0 (Metzger et al., 2007; Pignatel et al., 2011). We speculate that the increase in leakage rate for the polydisperse cases with large N_0 is a consequence of the disturbance to the heavy particles caused by relative motion with the lighter particles. The cases with large N_0 values are more susceptible to these disturbances because the light particles remain in the droplet for a longer time period than is the case with smaller values of N_0.

Cases in which the suspension droplet dynamics is dominated by hydrodynamic interaction between the particles are of particular interest, since these cases provide an illustration of the ability of hydrodynamic interaction to inhibit particle segregation. To explore such problems further, results are reported for a series of computations with different values of β, but with all other parameters fixed to the same values as used for the simulation shown in figure 4. The average particle fall velocity $v^*_{ave} = -dy^*_{ave}/dt^*$ is plotted as a function of time in figure 6a for values of β ranging between 0.1 and 0.9. This velocity is computed separately for the light and heavy particles, which are plotted in figure 6a using dashed and solid curves, respectively. The fall velocity of all particles reaches a maximum value at about $t^* = 0.4$, with roughly the same value for both light and heavy particles. The value of v^*_{ave} decreases with time after this peak value is achieved, which is associated with the decrease in number of particles in the droplet as a result of tail formation. Because the light particles have a greater tendency to move into the tail than do the heavy particles, the average fall velocity of the light particles decreases with time more quickly than for the heavy particles. Since the isolated particle

fall velocity (and hence also the fall velocity of particles in the tail) decreases with decrease in particle density ρ_n, the average fall velocity of the light particles in figure 6a decreases as β increases. For the case with $\beta = 0.9$, the light particles have lower density than the surrounding fluid and the long-time value of v^*_{ave} for these particles is negative (indicating that the particles rise upward in the fluid). The fall velocity for the heavy particles is observed to have a similar value for all values of β examined.

The degree of particle spread in the vertical direction is quantified using the root-mean-square position of the particles in the *y*-direction, y^*_{rms}, which is plotted as a function of time in figure 6b. Small values of y^*_{rms} can be achieved either if particles all remain in the droplet or if particles are quickly removed from the droplet and pass into the tail. The largest values of y^*_{rms} occur when particles move very slowly from the droplet into the tail. The rate of passage of the light particles from the droplet into the tail can be quantified by plotting the percentage of the initial light particles that remain in the droplet as a function of time, shown in figure 6c. The results indicate a monotonic increase in the segregation rate as the value of β increases.

By observing the difference in the value of y^*_{rms} for the heavy and light particles in figure 6b, we can infer the different extent to which the two types of particles have become spread out into the droplet tail. For the case with $\beta = 0.1$, there is only a slight difference in density between the two particles types, and the values of y^*_{rms} in figure 6b consequently remain fairly close to each other, with the y^*_{rms} values for the lighter particles slightly higher due to their greater tendency to pass into the droplet tail. Cases with β values ranging from 0.3 to 0.9 exhibit very different values of y^*_{rms} between the

two particle types. For the heavy particles, particles with densities closest to the nominal density (small β) have the smallest values of y^*_{rms}, and particles with higher densities (larger β) have larger values of y^*_{rms}. A similar trend holds during the initial part of the calculation for the lighter particles. However, as time progresses the value of y^*_{rms} for the light particles is observed to asymptote to a nearly constant value. Both this asymptotic value and the time at which this flattening of the y^*_{rms} curve occurs decrease as β increases. In this asymptotic state, all of the lighter particles have been removed from the droplet and passed into the tail. Since all of the light particles in the tail fall at approximately the same speed, the value of y^*_{rms} for the light particles remains approximately constant in this state.

There are numerous mixing and segregation indices used in the literature, many of which are adopted for specific problems (Li and McCarthy, 2005; Jain et al., 2005). A mixing index proposed for DEM simulations by Amar et al. (2002) would seem to be applicable for the problem addressed in the current paper. In this paper, a *generalized mean mixing index* is defined for a given coordinate direction (say, *y*) as

$$G_i = \left[\frac{1}{N_i} \sum_{j=1}^{N_i} (y_j - y_{ref}) \right] \Big/ \left[\frac{1}{N_{tot}} \sum_{k=1}^{N_{tot}} (y_k - y_{ref}) \right], \qquad (9)$$

where y_{ref} is taken as the minimum value of *y* occupied by any of the particles. The numerator of (10) is a sum over all N_i particles of type *i*, whereas the denominator is a sum over all N_{tot} particles in the system. A value of *G* equal to 1 indicates that particle

type i is distributed within the solution domain in a similar manner to all of the other particles. A value of G less than 1 indicates that particles of type i tend to have lower value of y than the average value for the entire particle set, and a value greater than 1 indicates that particles of type i tend to have higher values of y than the average value for the entire particle set.

The mixing measure G_{light} for the light particles is plotted as a function of time for different values of β in figure 6d. The initial value of G_{light} is equal to unity for all cases, indicating that the initial condition is well mixed. For small values of t^*, the value of G_{light} increases with time as the lighter particles preferentially segregate into the droplet tail. At some point around $t^* \approx 1.5$, a maximum value of G_{light} is attained, after which the mixing measure gradually decreases for the remainder of the computation as the heavier particles begin to enter into the droplet tail in larger numbers. For $\beta \leq 0.5$, the value of the mixing measure is found to exhibit a marked increase with increase in β, indicating that the extent of particle segregation becomes substantially greater as the density difference between the particles increases. The trend breaks down for $\beta > 0.5$, where we notice that the three cases with $\beta = 0.5$, 0.7, and 0.9 all have similar values of the mixing measure.

3. Experimental Method and Results

3.1. Experimental Method

A series of experiments were conducted in which a particle suspension droplet settles in a container filled with a transparent fluid. A diagram of the experimental set-up

is given in figure 7. The vessel used in the experiments has inner cross sectional dimensions of 9 cm by 9 cm, and was filled with the working fluid to a height of 28 cm. The fluid used in the experiments consisted of a mixture of water-soluble UCONN oil and water to create a fluid with a kinematic viscosity of 174×10^{-6} m^2/s and a density of 0.95 g/cm^3. The container was lit from the side with white light from four 6400K fluorescent tubes. A ruler with millimeter scale spanning the container height was attached to the other side, and the container was placed in front of a black background. The video camera used to capture the images of the falling droplet was a Sony HDR-SR12 with a frame rate of 30 frames per second.

Combinations of four different types of spherical particles were used in the experiments, the characteristics of which are given in table 1. The particle size distributions were measured using a digital imaging system (Image Pro Plus 6.0, Media Cybernetics), where the diameter given in the table is the mean diameter and the uncertainty stated is equal to one standard deviation, with sample sizes between 70-100 particles. The particle density was calculated by measuring the mass of a sample of particles and dividing it by the measured volume of the same sample. The mass was measured with a scale that has a precision of 0.0001 grams, and the volume was measured by putting the sample into a graduated cylinder with a 0.2 ml scale and adding a known volume of water into the graduated cylinder. The error in the density value that is given is calculated using the standard error propagation equation from the known uncertainty of the mass and volume measurements. The measured values of both the particle diameters and densities were found to be consistent with manufacturer specified values. The terminal settling velocity of each particle is determined by measuring the

position and time from a series of time-stamped photos pulled from a video of the falling particle, with a time precision of $0.03\,\mathrm{s}$ and a length precision of 1 mm. The average particle velocity is calculated by averaging the velocity from 20 samples, and the uncertainty is equal to one standard deviation from the mean.

The particle suspension was formed by first measuring out the two sets of particles to be used in the given experiment. The particle number ratio N_1 / N_2 for all of the experiments was set equal to 1. To estimate particle number, tweezers were used to count out 100 particles of each particle type, and the mass of the 100 particles was recorded with an accuracy of $0.0001\,\mathrm{grams}$. Using these values, the number of particles in a sample was obtained by measuring the sample's mass and dividing by the mass per particle. Once an equal number of particles of each type were measured, both sets of particles were put in a small closable container and the container was vigorously shaken. The particles were then put into a syringe with a 4 mm diameter opening and, with the syringe extended to leave empty space for mixing, the syringe was vigorously shaken to ensure that the particles were well mixed. Fluid from the vessel was then added to the particles in the syringe, and the syringe was vigorously shaken again to ensure an even distribution of the two types of particles within the suspension. The particle suspension was injected into the fluid in the test vessel by holding the syringe vertically with the syringe tip about 1cm above the surface of the fluid. The suspension was manually injected into the container by applying slight pressure to the syringe causing a droplet to slowly form at the end of the syringe. The droplet falls into the fluid when the weight of the droplet exceeds the surface tension force between the droplet and the syringe.

The number of particles in the suspension droplet was estimated by measuring the mass of a series of droplets that were dripped onto a surface, using the same approach for droplet generation as used in the experiments. Sample sizes of 21, 20, and 28 were used for experiment sets 1, 2, and 3 respectively. The known droplet concentration was then used to calculate the approximate number of each particle type in each sample droplet. The average total number of particles in a droplet and the associated root-mean square uncertainty were computed from the sample, giving the values listed in table 2. Each droplet consisted of approximately even amounts of N_1 and N_2, with an uncertainty equal to half of the uncertainty for N_0 listed in table 2.

3.2. Experimental Results

Experimental runs were first performed in a vessel filled with a lower viscosity fluid to examine the evolution of a suspension droplet with much lower particle concentration. The lower viscosity fluid allowed for the falling particles to spread out more with the initial impact and form a suspension droplet with a much lower initial concentration. Similar to what was observed in the computations with low particle concentrations (figure 5), the two types of particles immediately start to separate from each other and there is no droplet tail formation. Because the particles are spread out from each other, there is significantly less hydrodynamic interaction between the falling particles, which is the driving mechanism for the tail formation.

As we are primarily interested in particle segregation in cases with significant particle hydrodynamic interaction, the primary focus of the experiments was on cases with sufficiently large particle concentration that the entire particle set settles downward

as a single droplet, with the exception of the thin tail that trails behind the droplet. Three sets of experiments were performed, with multiple runs performed for each set. The characteristics of each set are listed in table 2. In experiment set 1, the particles have the same density but different particle radii. In experiment set 2, the particles have nearly the same radius, but different densities. In experiment set 3, both the particle radius and density are different. The mean values of L and Re_d were determined by averaging results from 5, 9, and 8 runs for experimental set numbers 1, 2, and 3, respectively. In some of the experimental runs, the droplet was initially teardrop shaped instead of spherical, as a result of its injection into the fluid in the vessel. In such cases, the particles that enter the fluid last are the ones contained in the rear of the teardrop, and are observed to quickly break apart from the droplet, leaving a roughly spherical droplet composed of the remaining particles. All of the experimental analysis starts with the droplet in this spherical shape, and does not include the particles that were separated from the droplet at the time of initial injection.

Runs with experimental set 1 were conducted to study the problem of a falling suspension droplet containing two different size particles, with $\alpha \equiv \left| r_{p2} - r_{p1} \right| / \bar{d} = 1.43$. Figure 8 shows a time series of photos of a the settling suspension droplet falling, where the large particles (red) are about 2.2 times larger than the small particles (gold). The tail that forms behind the droplet consists of both small and large particle sizes, but the small particles are more numerous in the tail region than the large particles. Runs with experimental set 2, shown in figure 9, were conducted to study the problem of a falling suspension droplet containing two different density particles, with $\beta = 0.067$. The heavy particles (silver) are 14% heavier than the light particles (red). The droplet tail contains

both heavy and light particles, but the light particles are significantly more numerous. Experimental set 3, shown in figure 10, compares particles with a substantial difference in both particle size and density, with $\alpha = 0.44$ and $\beta = 0.473$. The tail behind the droplet consists of only smaller/lighter particles for the initial part of the run, until eventually one larger/heavier particle enters the tail.

Plots of the droplet fall velocity with time are shown in figure 11a for experiment sets 1-3. To calculate the velocity, position and time data are obtained from a series of time-stamped video photos with a time precision of $0.03\,\mathrm{s}$ and a length precision of 1 mm. The uncertainty of the experimental droplet fall velocity is computed using the standard propagation of error equation from the measured uncertainty in the change in particle distance and the change in time, and is found to be 1.0 mm/s, 1.0 mm/s, and 8.7 mm/s for sets 1, 2, and 3, respectively. The droplet velocity decreases with time, as was also observed in the computations, due to the loss of particles from the droplet as the particles migrate into the tail.

The percentage of each particle type that is contained in the tail was calculated as a function of time. The uncertainty in the time is $0.03\,\mathrm{s}$, and the uncertainty in the particle count is 1 particle. The experimental values varied significantly between different runs from the same experimental set due to variation in the initialization of the droplets. The mean values are plotted in figure 12a-c for all of the experiment sets. Standard deviation of these values are recorded as 3.0 for the dashed line and 5.5 for the solid line in figure 12a, 6.4 for the dashed line and 3.1 for the solid line in figure 12b, and 10.3 for the dashed line and 1.5 for the solid line in figure 12c. Similar large variation between runs of the same set also occurred in the experiments of Metzger et al. (2007). The plots in

figure 12 confirm the experimental observation that the lighter/smaller particles were the dominant particles in the tail, and the percentage of larger/heavier particles in the tail decreases with increasing values of β and α.

The experimental droplet fall velocity was divided by the theoretical solution (8) and is plotted with time in figure 11b. The droplet fall velocity is non-dimensionalized by dividing by the average isolated particle settling speed for the different particle types that make up the droplet. These isolated settling speeds were obtained empirically, and are listed in table 2. The droplet diameter is measured with digital imaging software and has an uncertainty of 1mm. The number of particles in the droplet with time is calculated by subtracting the number of particles counted in the tail at that time from the initial number of particles in the droplet. The uncertainty of the experimental droplet fall velocity divided by the theoretical solution (8) is computed using the standard propagation of error equation from the measured uncertainty in the fall velocity and the number of particles, and is found to be 0.16, 0.03, and 0.25, for sets 1, 2, and 3, respectively. Figure 11b shows that the value of the experimental droplet fall velocity divided by the theoretical solution remains approximately constant with time at mean values of approximately 0.65, 0.58, and 0.85 for sets 1, 2, and 3, respectively. The experimental values of this velocity ratio are close to the value obtained computationally using the oseenlet-based method, as shown in figure 2c.

4. Conclusions

An investigation of segregation of polydisperse particles of different sizes and densities in a settling suspension droplet was performed using both computations and

experiments. The computations approximated the particle hydrodynamic interaction using an oseenlet-based simulation method that allows finite (non-small) values of the flow Reynolds number, while still requiring that the particle Reynolds number is small. The experiments were conducted by observing the fall of suspension droplets formed of binary particle mixtures consisting of particles with different sizes and densities in a viscous fluid.

The particle hydrodynamic interactions are of primary importance for the flow of concentrated suspension droplets, for which the droplet settling speed is approximately an order of magnitude larger than that of an isolated particle. The computed fall velocity of the suspension droplet was compared against an approximate theoretical solution, and the ratio of the computed to the theoretical values of droplet fall velocity are found to be consistent with both experimental results from our study and with experimental and computational solutions obtained by other investigators. Dynamics of bidisperse suspension droplets depends strongly on the particle concentration. For low concentrations, the amount of particle hydrodynamic interaction is insufficient to oppose the gravitational separation of the particles, and the particle type with larger terminal velocity quickly pulls away from the slower particles, leaving a deformed cloud of the slower particles behind. When the particle concentration is sufficiently large, the particle hydrodynamic interaction is sufficient to hold particles of both types together within the suspension droplet, thus inhibiting particle separation and allowing the droplet to settle as a single unit.

The current paper provides a detailed examination of suspension droplet dynamics under conditions where strong particle hydrodynamic interaction holds the particle

mixture together into one suspension droplet. As was observed previously for monodisperse droplets, a falling suspension droplet with high concentration develops a thin tail of trailing particles which slowly leak out from the rear portion of the droplet. A novel segregation mechanism is observed to occur by which the particles with smaller terminal velocity have a preferential tendency to be transported into the droplet tail, whereas particles with higher terminal velocity have a higher tendency to remain within the suspension droplet. Three different stages of particle segregation are observed – the first in which only the slower particles are transported into the tail, the second with a mixture of particles of different sizes/densities transported into the tail (but still dominated by the slower particles), and the final stage in which all remaining particles in the droplet are of the type with faster terminal velocity.

The essential problem examined in this paper concerns the inhibition of particle segregation by the hydrodynamic interaction of the particles in a situation where the particle terminal velocity differs within the mixture. This difference in terminal velocity acts to try to pull apart the mixture (enhancing segregation), whereas the hydrodynamic interaction acts to hold the mixture together (suppressing segregation). However, even in cases with strong hydrodynamic interaction, segregation still occurs within certain regions of the mixture near the edges of the suspension droplet, and particularly near the droplet rear stagnation point. This basic problem occurs in many different particulate flow problems in which particle agglomerates or clusters are transported relative to the surrounding fluid. The model problem examined in the current paper should provide insight into the ability of clusters formed of a mixture of different particle sizes and

densities to hold their structure even in the presence of differences in drag and other fluid forces, which attempt to tear the cluster apart.

Acknowledgements

The work of JSM and MF was supported by NASA EPSCoR under projects NNX07AK92A and NNX08AZ07A and by the U.S. National Science Foundation under projects CBET-1332472 and DGE-1144388. The work of SL and MY was supported by the National Natural Science Funds of China (No. 50976058).

References

Adachi, K., Kiriyama, S. & Yoshioka, N. 1978 The behavior of a swarm of particles moving in a viscous fluid. *Chemical Engineering Science* **33**(1), 115-121.

Asmar, B.N., Langston, P.A. & Matchett, A.J. 2002 A generalised mixing index in distinct element method simulation of vibrated particulate beds. *Granular Matter* **4**, 129-138.

Bosse, T., Kleiser, L., Härtel, C. & Meiburg, E. 2005 Numerical simulation of finite Reynolds number suspension drops settling under gravity. *Physics of Fluids* **17**, 037101.

Bretherton, F.P. 1964 Inertial effects on clusters of spheres falling in a viscous fluid. *Journal of Fluid Mechanics* **20**(1), 401-410.

Chen, H. & Marshall, J.S. 1999 A Lagrangian vorticity method for two-phase particulate flows with two-way phase coupling. *Journal of Computational Physics* **148**, 169-198.

Cundall, P.A. & Strack, O.D.L. 1979 A discrete numerical model for granular assembles. *Geotechnique* **29**(1), 47-65.

Ekiel-Jeżewska, M.L. & Felderhof, B.U. 2005 Periodic sedimentation of three particles in periodic boundary conditions. *Physics of Fluids* **17**, 093102.

Ekiel-Jeżewska, M.L. & Felderhof, B.U. 2006a Clusters of particles falling in a viscous fluid with periodic boundary conditions. *Physics of Fluids* **18**, 121502.

Ekiel-Jeżewska, M.L., Metzger, B. & Guazzelli, É. 2006b Spherical cloud of point particles falling in a viscous fluid. *Physics of Fluids* **18**, 038104.

Elghobashi, S. & Truesdell, G.C. 1993 On the two-way interaction between homogeneous turbulence and dispersed solid particles. I: Turbulence modification. *Physics of Fluids A* **5**, 1790-1801.

Faletra, M. 2014 Segregation of particles of variable size and density in falling suspension droplets. M.S. Thesis, The University of Vermont, Burlington.

Hadamard, J. 1911 Movement permanent lent d'une sphere liquide visqueuse dans un liquid visqueux. *C.R. Acad. Sci. Paris Sér. A-B* **152**, 1735-1739.

Hertz, H. 1882 Über die Berührung fester elastische Körper. *J. reine und angewandte Mathematik* **92**, 156-171.

Hocking, L.M. 1964 The behaviour of clusters of spheres falling in a viscous fluid. Part 2. Slow motion theory. *Journal of Fluid Mechanics* **20**, 129-139.

Hurley, P. & Physick, W. 1993 Lagrangian particle modelling of buoyant point sources: Plume rise and entrapment under convective conditions. *Atmospheric Environment A* **27**(10), 1579-1584.

Jain, N., Ottino, J.M. & Lueptow, R.M. 2005 Regimes of segregation and mixing in combined size and density granular systems: an experimental study. *Granular Matter* **7**, 69-81.

Jayaweera, K.O.L.F., Mason, B.J. & Slack, G.W. 1964 The behaviour of clusters of spheres falling in a viscous fluid. Part 1. Experiment. *Journal of Fluid Mechanics* **20**(1), 121-128.

Joseph, G.G., Zenit, R., Hunt, M.L. & Rosenwinkel, A.M. 2001 Particle-wall collisions in a viscous fluid. *Journal of Fluid Mechanics* **433**, 329-346.

Kojima, M., Hinch, E.J. & Acrivos, A. 1984 The formation and expansion of a toroidal drop moving in a viscous fluid. *Physics of Fluids* **27**(1), 19-32.

Li, H. & McCarthy, J.J. 2005 Phase diagrams for cohesive particle mixing and segregation. *Physical Review E* **71**, 021305.

Machu, G., Meile, W., Nitsche, L.C. & Schaflinger, U. 2001 Coalescence, torus formation and breakup of sedimenting drops: experiments and computer simulations. *Journal of Fluid Mechanics* **447**, 299-336.

Marshall, J.S. 2009 Discrete-element modeling of particulate aerosol flows. *Journal of Computational Physics* **228**, 1541-1561.

Marshall, J.S. & Sala, K. 2013 Comparison of methods for computing the concentration field of a particulate flow. *International Journal of Multiphase Flow* **56**, 4-14.

Martonen, T.B. 1992 Deposition patterns of cigarette-smoke in human airways. *American Industrial Hygiene Association Journal* **53**, 6-18.

Metzger, B., Nicolas, M. & Guazzelli, É. 2007 Falling clouds of particles in viscous fluids. *Journal of Fluid Mechanics* **580**, 283-301.

Nitsche, J.M. & Batchelor, G.K. 1997 Break-up of a falling drop containing dispersed particles. *Journal of Fluid Mechanics* **340**, 161-175.

Noh, Y. & Fernando, H.J.S. 1993 The transition in the sedimentation pattern of a particle cloud. *Physics of Fluids A* **5**(12), 3049-3055.

Park, J., Metzger, B., Guazzelli, É. & Butler, J.E. 2010 A cloud of rigid fibres sedimenting in a viscous fluid. *Journal of Fluid Mechanics* **648**, 351-362.

Phalen, R.F., Oldham, M.J., Mannix, R.C. & Schum, G.M. 1994 Cigarette-smoke deposition in the tracheobronchial tree - evidence for colligative effects. *Aerosol Science and Technology* **20**, 215-226.

Pignatel, F., Nicolas, M. & Guazzelli, É. 2011 A falling cloud of particles at a small but finite Reynolds number. *Journal of Fluid Mechanics* **671**, 34-51.

Proudman, I. & Pearson, J.R.A. 1957 Expansions at small Reynolds numbers for the flow past a sphere and a circular cylinder. *Journal of Fluid Mechanics* **2**(3), 237-262.

Robinson, R.J. & Yu, C.P. 2001 Deposition of cigarette smoke particles in the human respiratory tract. *Aerosol Science and Technology* **34**, 202-215.

Roeder, R.K., Steinlage, G.A., Trumble, K.P. & Bowman, K.J. 1995 Preventing segregation during centrifugal consolidation of particulate suspensions: particle drafting. *Journal of the American Ceramic Society* **78**(9), 2367-2373.

Rybczynski, W. 1911 Über die fortschreitende Bewegung einer flüssigen Kugel in einem zähen Medium. *Bull. Int. Acad. Sci. Cracov*. **1911A**, 40-46.

Shinohara, K. & Golman, B. 2002 Segregation indices of multi-sized particle mixtures during the filling of a two-dimensional hopper. *Advanced Powder Technology* **13**(1), 93–107.

Subramanian, G. & Koch, D.L. 2008 Evolution of clusters of sedimenting low-Reynolds-number particles with Oseen interactions. *Journal of Fluid Mechanics* **603**, 63-100.

Tsuji, Y., Tanaka, T. & Ishida, T. 1992 Lagrangian numerical simulation of plug flow of cohesionless particles in a horizontal pipe. *Powder Technology* **71**, 239-250.

Vasseur, P. & Cox, R.G. 1977 The lateral migration of spherical particles sedimenting in a stagnant bounded fluid. *Journal of Fluid Mechanics* **80**(3), 561-591.

Walther, J.H. & Koumoutsakos, P. 2001 Three-dimensional vortex methods for particle-laden flows with two-way coupling. *Journal of Computational Physics* **167**, 39-71.

Figure Captions

Figure 1. Plot showing formation of tail behind a falling monodisperse suspension droplet with $\mathrm{Re}_d = 1.4$. Images are shown at times (a) $t^* = 0$, (b) 0.2, (c) 0.4, (d) 0.6 and (e) 0.8.

Figure 2. Time variation of (a) the dimensionless droplet fall velocity, (b) the number of particles remaining in the droplet, and (c) the ratio of the average droplet fall velocity to the theoretical estimate (16). The plots are for monodisperse particles with droplet Reynolds numbers $\mathrm{Re}_d = 1.4$. The dashed line in (c) corresponds to the theoretical HR solution given by Eq. (8).

Figure 3. Plot showing the time variation of the root-mean-square y-position (solid line) and the value of $(y^*_{\max} - y^*_{\min})/4$ (dashed line) for a monodisperse droplet.

Figure 4. Time series of a droplet with $N_0 = 300$, showing preferential leakage of lighter particles into the droplet tail, for a case with particles with two densities with $\beta = 0.5$. Images are shown at times (a) $t^* = 0$, (b) 0.2, (c) 0.4, (d) 0.6 and (e) 1.0. The light particles are shown in blue and the heavy particles in red.

Figure 5. Percentage of initial particles remaining in the droplet as a function of dimensionless time for different values of the initial particle number N_0. Heavy particles (solid lines) and light particles (dashed lines) are shown for a series of cases with $\beta = 0.5$ and $\mathrm{Re}_d = 1.4$. Colors correspond to cases with $N_0 = 50$ (red), 100 (green), 300 (blue), and 1000 (black).

Figure 6. Effect of density difference on time variation of (a) the average fall velocity, (b) the root-mean-square value of y, (c) percentage of light particles remaining in the droplet (based on total number initially in droplet), and (d) mixing measure G_{light} for the light particles. Results in (a) and (b) are shown for both the heavy particles (dark lines) and the light particles (dashed lines) with $N_0 = 300$. Curves are shown for β values of 0.1 (red lines, A), 0.3 (green lines, B), 0.5 (blue lines, C), 0.7 (orange lines, D), and 0.9 (black lines, E).

Figure 7. Diagram of the experimental set-up including (A) the black background, (B) the injection syringe, (C) the lighting system, (D) the video camera, (E) the ruler, and (F) the vessel.

Figure 8. Photo of the particle positions of a falling droplet, with initial droplet diameter $L = 3.8\,\mathrm{mm}$, in experimental set 1 at dimensional times (seconds): (a) $t = 0$, (b) $t = 0.8$, (c) $t = 1.8$, (d) $t = 3.8$, and (e) $t = 4.3$. The large particles (red) are about 2.2 times larger than the small particles (gold).

Figure 9. Photos of the particle positions of a falling droplet with initial droplet diameter $L = 4\,\text{mm}$ in experimental set 2 at dimensional times (seconds): (a) $t = 0$, (b) $t = 1.2$, (c) $t = 2.7$, and (d) $t = 4.2$. The heavy particles (silver) are 14% heavier than the light particles (red).

Figure 10. Photos of the particle positions of a falling droplet with initial droplet diameter $L = 3.5\,\text{mm}$ in experimental set 3 at dimensional times (seconds): (a) $t = 0$, (b) $t = 0.44$, (c) $t = 0.94$, (d) $t = 1.4$, and (e) $t = 1.74$. The large/heavy particles (silver) are 27% larger and 3.2 times heavier than the small/light particles (red).

Figure 11. (a) Experimental droplet fall velocity versus time for experimental set 1 (squares), set 2 (circles), and set 3 (triangles). The lines are fits to the data. (b) Droplet fall velocity divided by the theoretical HR solution in Eq. (8).

Figure 12. Plots showing the percentage p_T of each type of particle contained in the vertical tail as a function of dimensionless time. Percentages are based on the total number of each type of particle for (a) experimental set 1, (b) set 2, and (c) set 3. Solid lines represent heavier (or larger) particles and dashed lines represent lighter (or smaller) particles.

Table 1. Characteristics of particles used in the experiments.

Particle Label	Material	Color	Diameter (mm)	Density (g/cm^3)	Isolated particle fall velocity (mm/s)
A	Glass	Gold	0.36 ± 0.03	2.44 ± 0.10	0.39 ± 0.1
B	Glass	Red	0.78 ± 0.05	2.55 ± 0.16	1.7 ± 0.3
C	Aluminum	Silver	0.77 ± 0.01	2.86 ± 0.35	2.1 ± 0.1
D	Chrome steel	Silver	0.96 ± 0.01	8.94 ± 1.9	13.0 ± 0.2

Table 2. Parameters characterizing the experimental data sets. The average values of the initial particle droplet diameter L, the droplet Reynolds number Re_d, and the initial number of particles N_0 are averaged over the different experimental runs.

Set #	Particles in Suspension	β	α	Avg. L (mm)	Avg. Re_d	$\overline{\rho}_p$ (g/cm^3)	$\overline{d}$ (mm)	Avg. N_0
1	A & B	0.022	1.43	4.1	0.69	2.495	0.61	156 ± 18
2	B & C	0.057	0.02	4.2	0.87	2.705	0.775	85 ± 10
3	B & D	0.556	0.24	3.7	1.94	5.75	0.87	44 ± 9

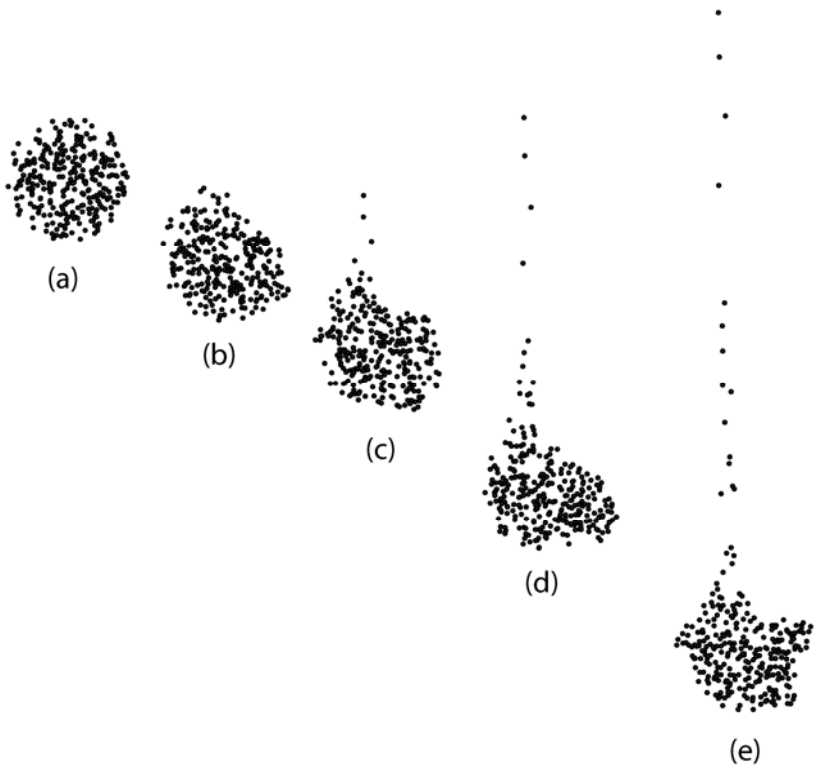

Figure 1. Plot showing formation of tail behind a falling monodisperse suspension droplet with $\mathrm{Re}_d = 1.4$. Images are shown at times (a) $t^* = 0$, (b) 0.2, (c) 0.4, (d) 0.6 and (e) 0.8.

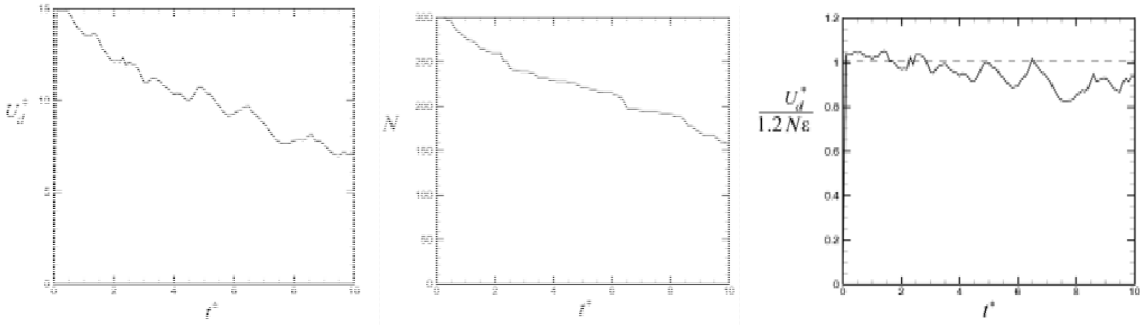

(a) (b) (c)

Figure 2. Time variation of (a) the dimensionless droplet fall velocity, (b) the number of particles remaining in the droplet, and (c) the ratio of the average droplet fall velocity to the theoretical estimate (16). The plots are for monodisperse particles with droplet Reynolds numbers $\mathrm{Re}_d = 1.4$. The dashed line in (c) corresponds to the theoretical HR solution given by Eq. (8).

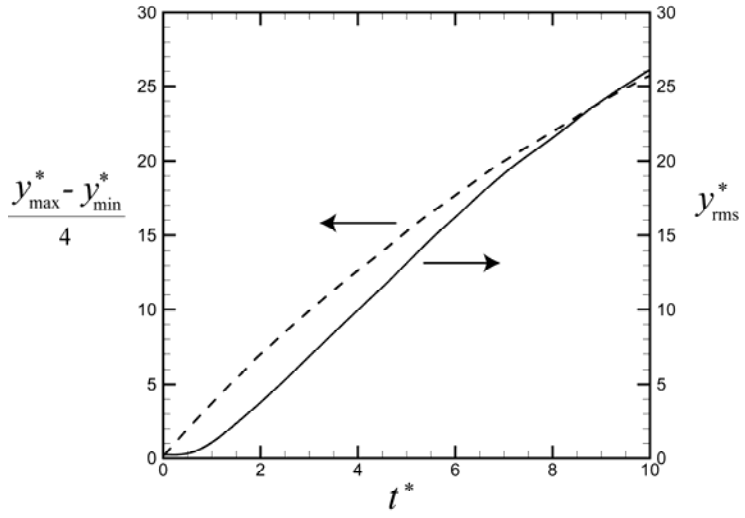

Figure 3. Plot showing the time variation of the root-mean-square y-position (solid line) and the value of $(y^*_{max} - y^*_{min})/4$ (dashed line) for a monodisperse droplet.

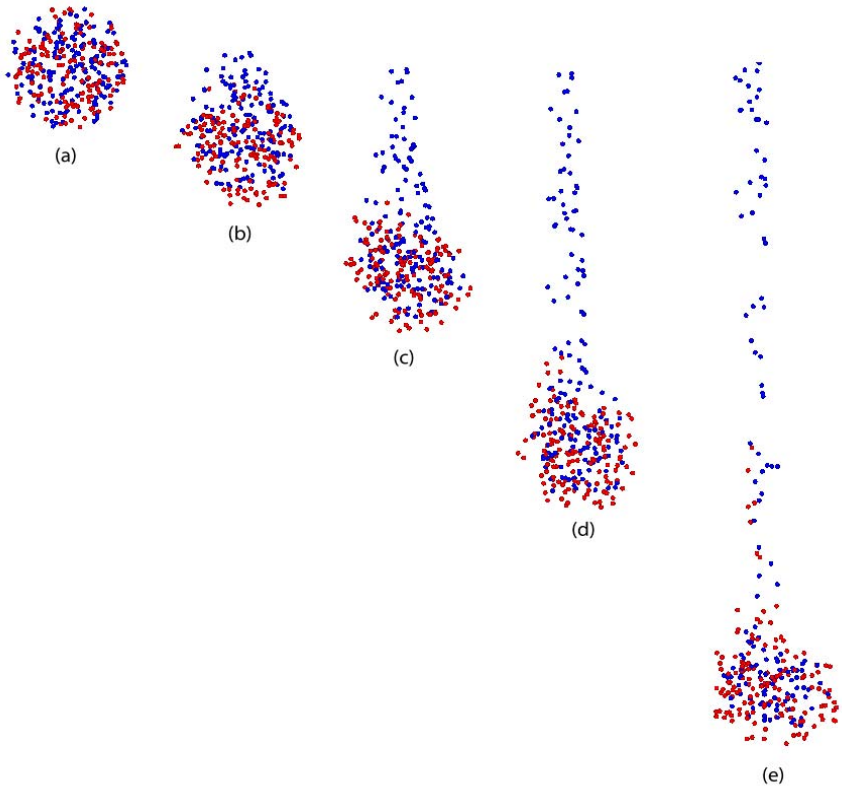

Figure 4. Time series of a droplet with $N_0 = 300$, showing preferential leakage of lighter particles into the droplet tail, for a case with particles with two densities with $\beta = 0.5$. Images are shown at times (a) $t^* = 0$, (b) 0.2, (c) 0.4, (d) 0.6 and (e) 1.0. The light particles are shown in blue and the heavy particles in red.

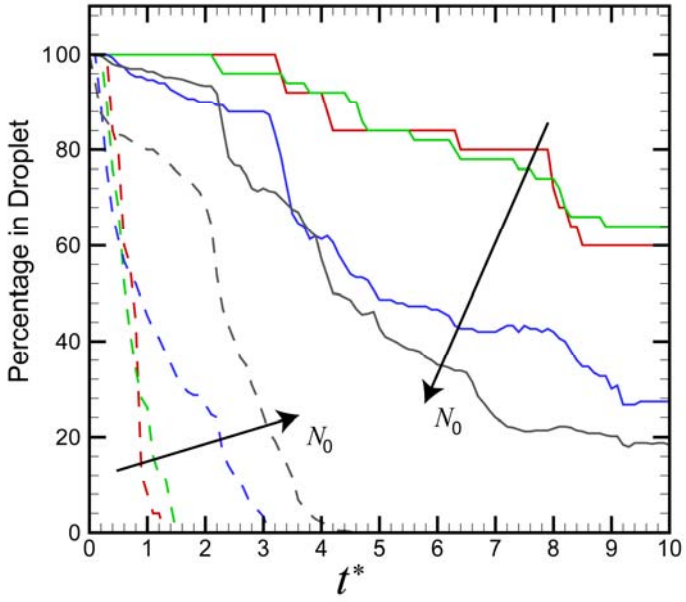

Figure 5. Percentage of initial particles remaining in the droplet as a function of dimensionless time for different values of the initial particle number N_0. Heavy particles (solid lines) and light particles (dashed lines) are shown for a series of cases with $\beta = 0.5$ and $\mathrm{Re}_d = 1.4$. Colors correspond to cases with $N_0 = 50$ (red), 100 (green), 300 (blue), and 1000 (black).

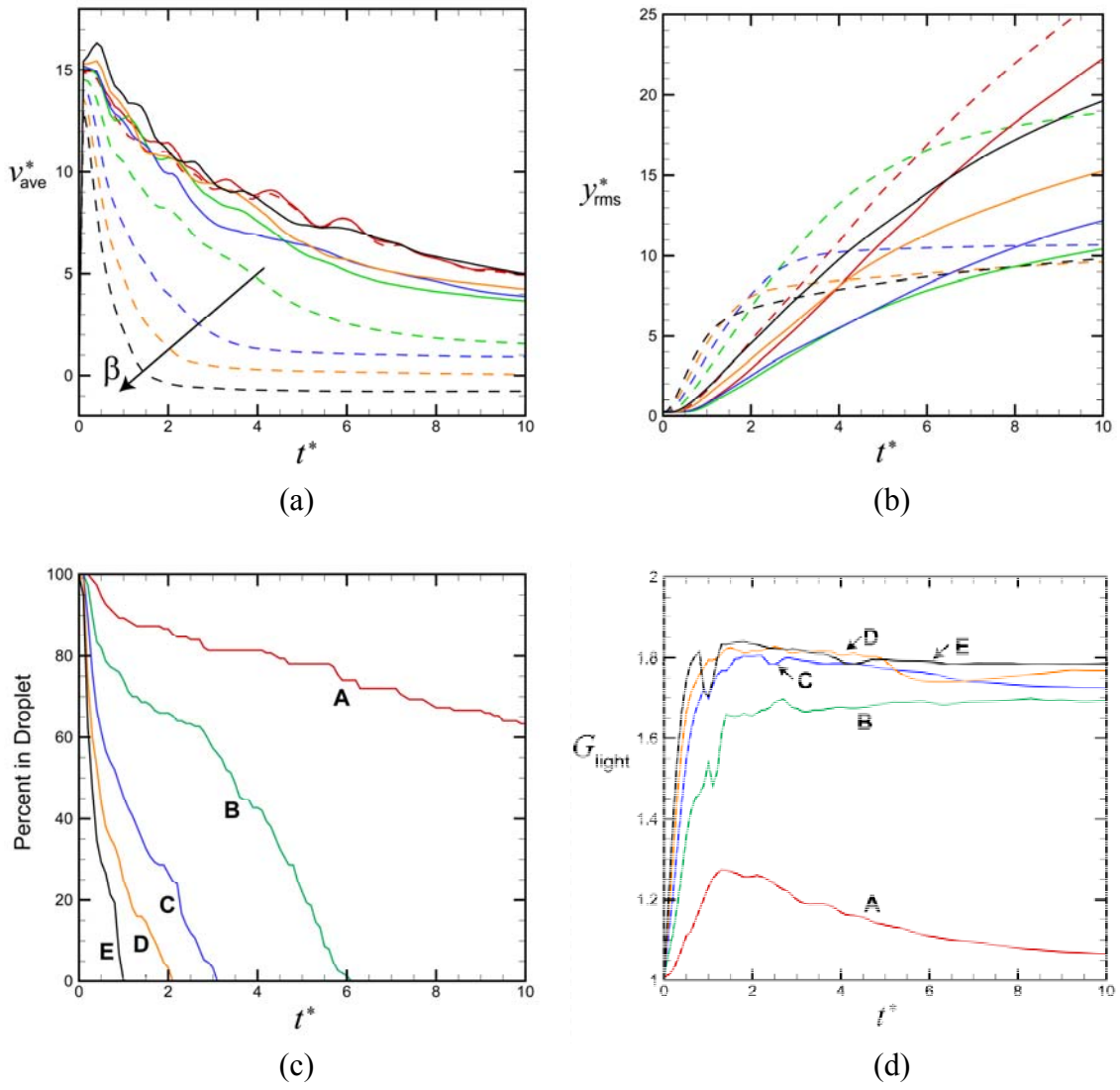

Figure 6. Effect of density difference on time variation of (a) the average fall velocity, (b) the root-mean-square value of y, (c) percentage of light particles remaining in the droplet (based on total number initially in droplet), and (d) mixing measure G_{light} for the light particles. Results in (a) and (b) are shown for both the heavy particles (dark lines) and the light particles (dashed lines) with $N_0 = 300$. Curves are shown for β values of 0.1 (red lines, A), 0.3 (green lines, B), 0.5 (blue lines, C), 0.7 (orange lines, D), and 0.9 (black lines, E).

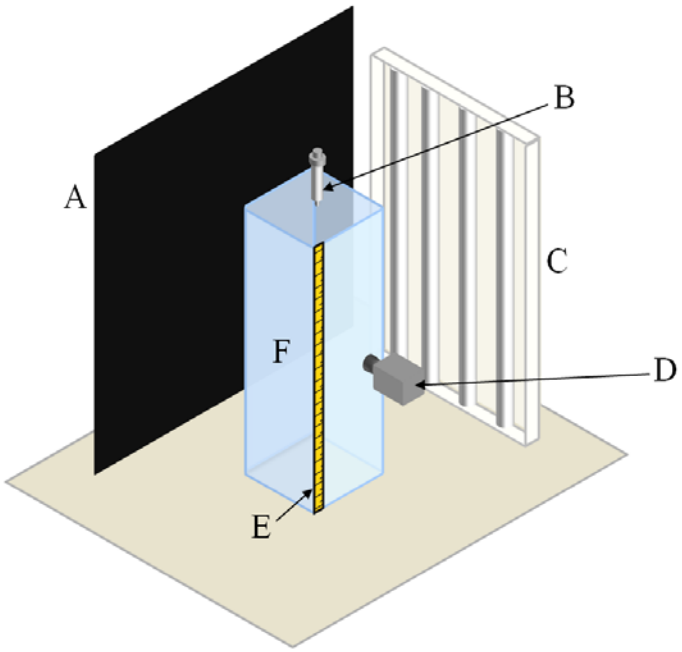

Figure 7. Diagram of the experimental set-up including (A) the black background, (B) the injection syringe, (C) the lighting system, (D) the video camera, (E) the ruler, and (F) the vessel.

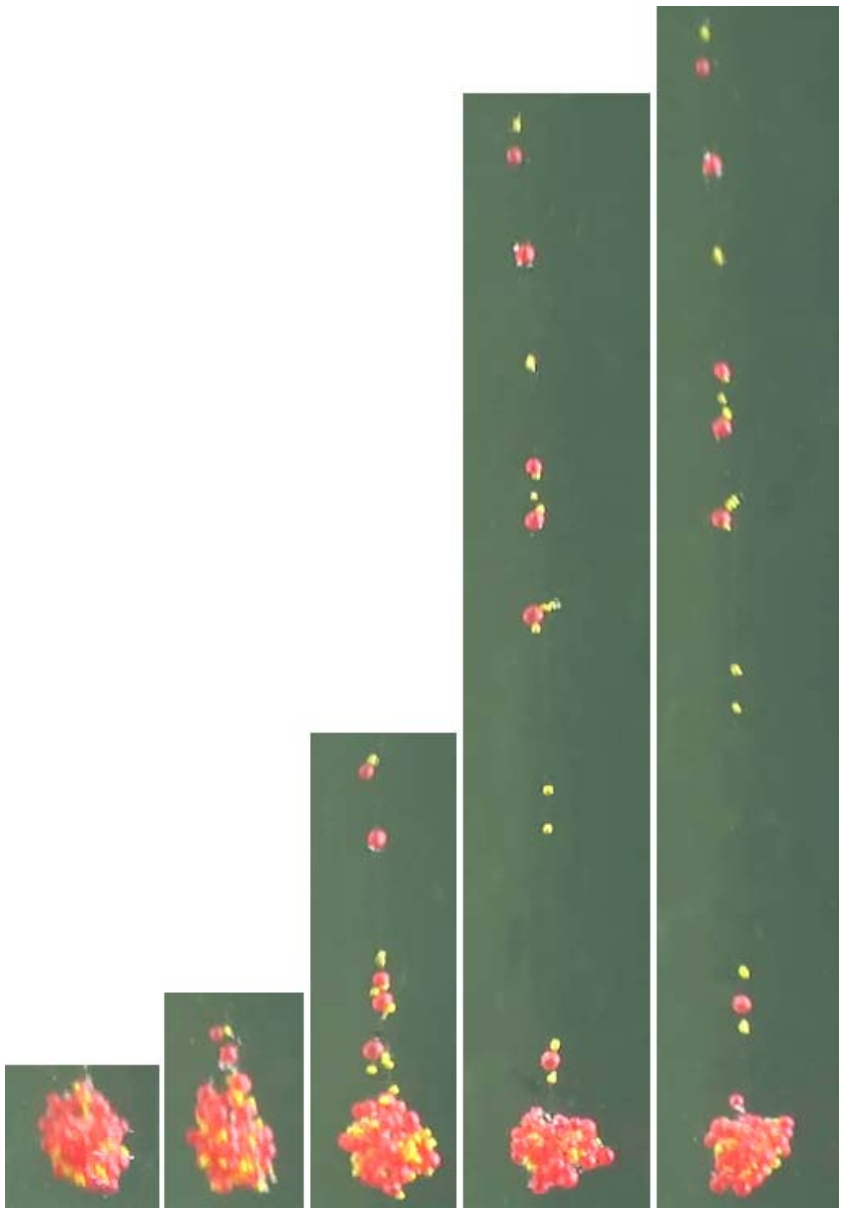

(a) (b) (c) (d) (e)

Figure 8. Photos of the particle positions of a falling droplet, with initial droplet diameter $L = 3.8\,\text{mm}$, in experimental set 1 at dimensional times (seconds): (a) $t = 0$, (b) $t = 0.8$, (c) $t = 1.8$, (d) $t = 3.8$, and (e) $t = 4.3$. The large particles (red) are about 2.2 times larger than the small particles (gold).

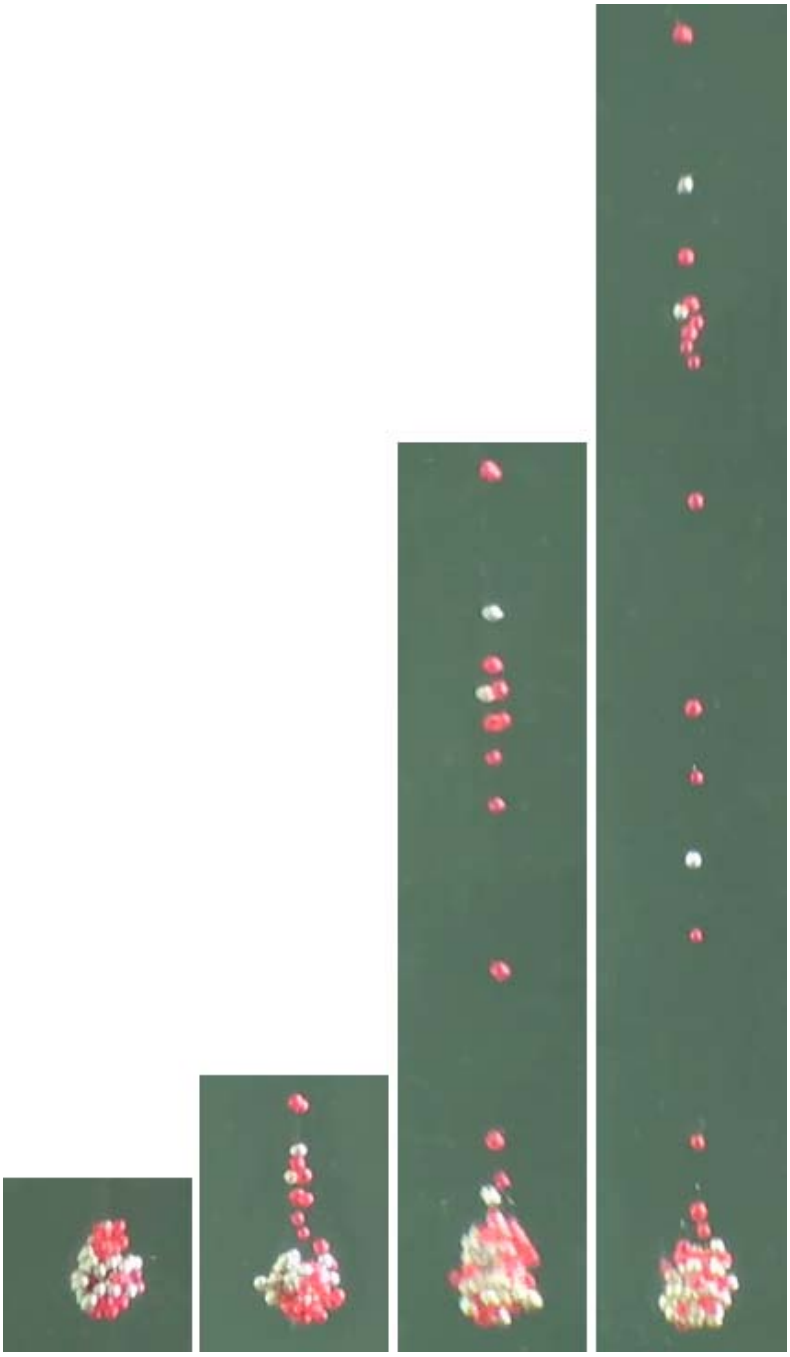

Figure 9. Photos of the particle positions of a falling droplet with initial droplet diameter $L = 4\,\text{mm}$ in experimental set 2 at dimensional times (seconds): (a) $t = 0$, (b) $t = 1.2$, (c) $t = 2.7$, and (d) $t = 4.2$. The heavy particles (silver) are 14% heavier than the light particles (red).

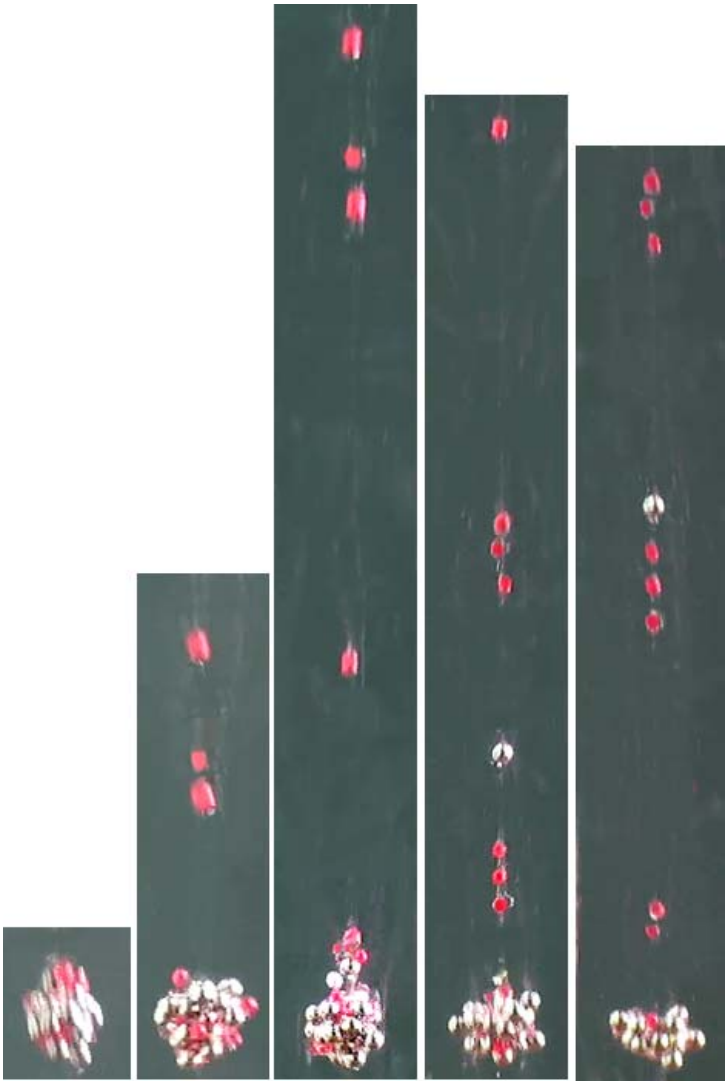

Figure 10. Photos of the particle positions of a falling droplet with initial droplet diameter $L = 3.5\,\text{mm}$ in experimental set 3 at dimensional times (seconds): (a) $t = 0$, (b) $t = 0.44$, (c) $t = 0.94$, (d) $t = 1.4$, and (e) $t = 1.74$. The large/heavy particles (silver) are 27% larger and 3.2 times heavier than the small/light particles (red).

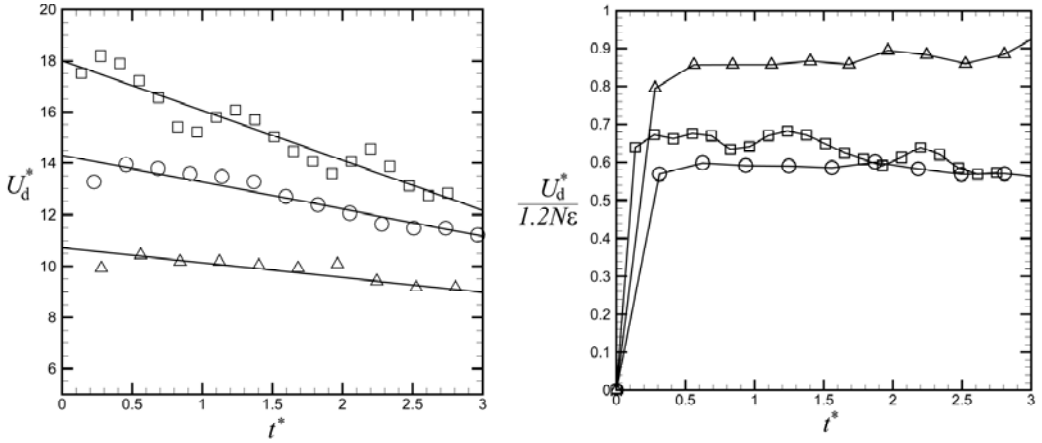

(a) (b)

Figure 11. (a) Experimental droplet fall velocity versus time for experimental set 1 (squares), set 2 (circles), and set 3 (triangles). The lines are fits to the data. (b) Droplet fall velocity divided by the theoretical HR solution in Eq. (8).

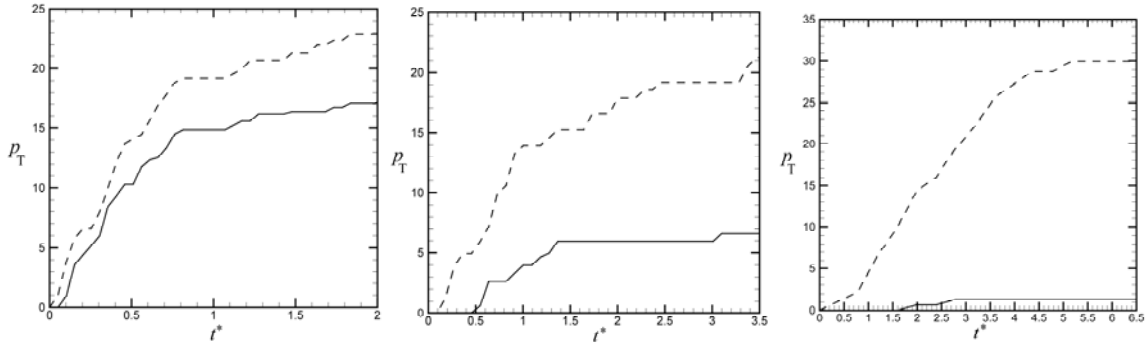

(a) (b) (c)

Figure 12. Plots showing the percentage p_T of each type of particle contained in the vertical tail as a function of dimensionless time. Percentages are based on the total number of each type of particle for (a) experimental set 1, (b) set 2, and (c) set 3. Solid lines represent heavier (or larger) particles and dashed lines represent lighter (or smaller) particles.